Extreme winds and precipitation during landfall of atmospheric rivers

Duane Waliser[1]* and Bin Guan[2]

Atmospheric rivers—long, narrow filaments of large integrated water vapour transport—are associated with weather and water extremes, such as precipitation extremes and flooding in western North America and northern Europe. Here we apply a global detection algorithm for atmospheric rivers to reanalysis data during 1997–2014 to investigate the impact of atmospheric rivers on wind extremes as well as precipitation extremes. We find that atmospheric rivers are associated with up to half of the extreme events in the top 2% of the precipitation and wind distribution, across most mid-latitude regions globally. Landfalling atmospheric rivers are associated with about 40–75% of extreme wind and precipitation events over 40% of the world's coastlines. Atmospheric rivers are associated with a doubling or more of the typical wind speed compared to all storm conditions, and a 50–100% increase in the wind and precipitation values for extreme events. We also find that the majority of extreme wind events catalogued between 1997 and 2013 over Europe with billion US dollar losses were associated with atmospheric rivers. We conclude that landfalling atmospheric rivers can represent a significant hazard around the globe, because of their association with not only extreme precipitation, but also extreme winds.

In recent years, there has been a growing interest in atmospheric rivers[1–5] (ARs), their regional impacts on water availability and flooding[6–9], their modulation by climate variability and change[10–15], and their representation in weather forecast models[16–18]. A vast majority of this interest has been focused on the hydrological component of ARs[3,6,7,10,11,19–21] (for example, moisture transport, precipitation, snowpack, flooding), with only a very limited number of global considerations[1,14,22]. In this study, we expand the consideration of ARs by quantifying their association with near-surface wind extremes in addition to precipitation, doing so with a global perspective, and with particular attention on AR landfalls at the world's coastlines. The emphasis on wind extremes, in addition to the more traditional hydrological considerations, is to highlight potential connections between ARs and other hazard and impact areas via wind (for example, storm surge and coastal flooding, wind damage, marine weather and significant wave height)[23–27].

Given that ARs are commonly defined by integrated water vapour transport (IVT), and wind is a necessary ingredient in the calculation of IVT, it is not completely unexpected for high winds to occur in conjunction with ARs. However, the fact that both wind and water vapour over the troposphere make up the definition of IVT, it is not obvious what the association is between extreme IVT, and thus ARs, and extreme near-surface winds. Moreover, since IVT is not a direct measure of precipitation, it is important to characterize the connection between extreme IVT and extreme precipitation. Quantifying these relationships addresses the following sorts of questions. What fraction of extreme wind events in a given part of the globe or coastal area occurs in conjunction with ARs? Are the very largest extreme wind events associated with AR events? Similar questions can be asked for extreme precipitation events. Moreover, what is the joint relationship between wind and precipitation extremes in a region heavily impacted by ARs? Finally, considering these relationships with associated economic information can yield answers to questions such as, how large are the financial losses for extreme wind events associated with ARs?

Impact of ARs globally

To illustrate the global impact of ARs on near-surface wind and precipitation extremes, we employ a recently developed global detection algorithm for ARs[14] which identifies ARs from 6-hourly IVT fields, in this case from ERA-Interim reanalysis, and examine their occurrence in relation to the frequency distribution of 10-m wind speed and surface precipitation values. See Methods and Supplementary Figs 1 and 2 for a description of the algorithm and the manner in which it is applied in this study. Figure 1a displays the global frequency of occurrence of ARs, with a value of 10% indicating that an AR occurs on average in that location about once every ten days. Figure 1b,c illustrates what fraction of extreme wind and precipitation events is associated with AR conditions, with the extreme values being defined as those above the 98th percentile[28] (see Supplementary Figs 3 and 4). Over much of the mid-latitudes, where the frequency of occurrence of ARs is relatively high, their connection with wind extremes is particularly high. In these regions, AR conditions occur in conjunction with wind extremes about 30–60% of the time. For example, over the mid-ocean regions of the Pacific, Atlantic and Indian oceans, AR conditions are associated with over 50% of the extreme wind events. Moreover, the southern stretches of Southern Hemisphere continents, western North America, northern Europe, southeast US, southern Greenland, and west central South America also exhibit high concurrence between ARs and extreme winds. The analogous map for precipitation closely mimics the same large-scale patterns and values.

Impact of ARs at landfall

Although the connection between ARs and wind extremes is most prominent in the mid-latitude ocean basins, and thus of importance to maritime weather considerations, equally important considerations are the impacts associated with AR landfalls[8,9,12,14,15,27,29]. Such landfalls are known to be associated with heavy precipitation extremes, but their relationship to wind extremes (and in turn the associated impacts such as

[1]Jet Propulsion Laboratory, California Institute of Technology, Pasadena, California 91109, USA. [2]Joint Institute for Regional Earth System Science and Engineering, University of California, Los Angeles, California 90095, USA. *e-mail: duane.waliser@jpl.nasa.gov

1

storm surge, wind hazards, coastal flooding), particularly from a global perspective, has not been quantified. Figure 2a combines and illustrates the information contained in the upper two maps of Fig. 1, but highlighting the values at the world's coastlines. This includes the frequency of occurrence of ARs in terms of days/year (circle size) and the fraction of extreme wind events—that is, those in the upper 2% of the frequency distribution—that are associated with AR conditions (shading). The results show that it is not uncommon for coastal areas, particularly in the mid-latitudes, to be impacted by ARs on 40 or more days per year, or about once every nine days with greater (lesser) occurrence expected in winter (summer)[14]. These AR occurrences in turn are associated with 25% or more of the wind extremes for many of the world's coastlines, and about 40 to 75% in 40% of the coastlines that are strongly influenced by AR conditions. For example, for western North America, northern Europe, New Zealand and southern South America, the results indicate that ARs occur on the order of 40 days per year (circle size), and these account for nearly half of extreme wind events (shading) that occur in the top 2% of the frequency distribution. Figure 2c provides the same information but for the precipitation (that is, combining information from the maps of Fig. 1a,c, but only at the coastlines). In this case, the spatial variabilities of the fractional value of extremes at the coastlines are similar between the precipitation and wind extremes.

To provide a more specific characterization of the relation between landfalling ARs and the very largest extremes and their associated values, Fig. 2b(d) shows the rank of the highest extreme wind (precipitation) value associated with an AR (circle colour) and the value of the wind speed (precipitation) (circle size) for that given extreme. Considering Fig. 2b, for example, coastal areas identified with red circles mean that an AR event was associated with the occurrence of the highest or second-highest wind extreme, based on the 6-hourly 10-m wind speed from the ERA-Interim reanalysis, in the 1997–2014 observation period analysed here. Similarly, yellow circles indicate that an AR event was associated with either the third-, fourth-, or fifth-highest wind extreme. The size of the circle indicates the value of the wind extreme in metres per second, with the top wind extremes being up to 50 m s^{-1} in some coastal regions. Note that comparisons between these reanalysis values which are grid-averaged and 6-hourly values have only a modest negative mean bias of about 0.5 m s^{-1} when compared against ocean and coastal buoys[30]. In addition, comparison with operational versions of the underlying forecast model of the reanalysis product, only a loose indicator of the potential bias in the reanalysis winds, indicates that the model underestimates the winds by about 10% at the highest values[31]. Thus, the actual value of the wind speed in these extremes as captured by this reanalysis is probably an underestimate[32], and a detailed assessment of these relationships for a given region would be best to rely on local wind gauge measurements.

Outside the deep tropics, it is not uncommon for ARs to be associated with the record value in the wind distribution, or at least an extreme ranking among the top five events, and that wind extreme values are very often over 15–20 m s^{-1}. This is found across the southern tier of the continents in the Southern Hemisphere and along almost the entire coastline of Antarctica, as well as the eastern, western and northern coasts of the continents in the Northern Hemisphere. The results in these figures emphasize the strong association of AR conditions with extreme wind events—or put another way, extreme winds typically do not occur in the absence of AR conditions. Similar relationships occur between AR occurrence and peak precipitation events. Note that the magnitude of the wind speed for the top-ranked values shown is roughly similar (within factor of 1) across the mid- and high latitudes, while the magnitude of the top-ranked values for precipitation are considerably smaller at high compared to low latitudes owing to the greatly reduced moisture capacity, and thus precipitation potential, for colder polar air.
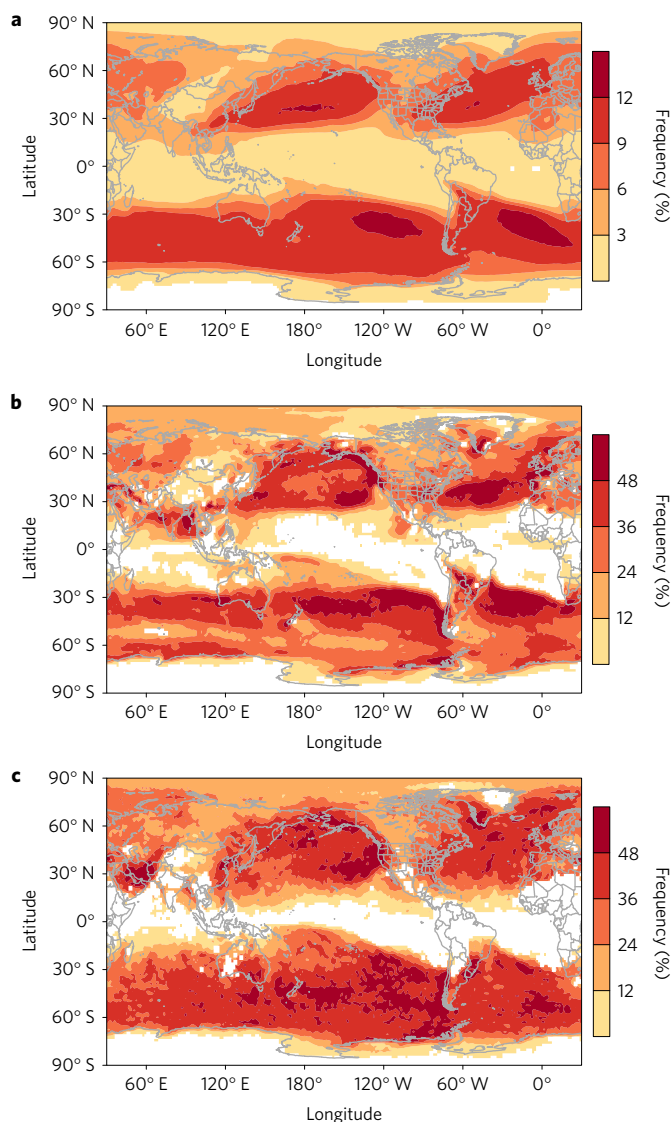

Figure 1 | AR fractions among wind and precipitation extremes. a, Map reflecting the frequency of global occurrence of AR events out of all time steps (that is, considering the entire distribution of wind/precipitation, including times with zero precipitation/wind)[14]. **b,c,** Global maps showing the frequency (% of times) that ARs are associated with surface (10 m) wind extremes (**b**) and surface precipitation extremes (**c**). In each case, extremes are defined as those exceeding the 98th percentile of non-zero values at a given grid cell. Note different colour scale for **a**. In **b** and **c**, values are shaded only if statistically significant at the 99% level; see Methods for details.

Impact of ARs on wind–precipitation histogram

To better understand, quantify and compare how AR conditions are related to the occurrence of wind and precipitation extremes, we examine joint histograms of wind speed versus precipitation. Combining information from the four regions outlined in Fig. 2 (blue boxes), indicative of high AR landfall frequency, Fig. 3(bottom left) shows the joint histogram of wind speed versus precipitation. In this case, the joint histogram is shown by the blue shading, with the blue lines in the plots above and to the right indicating the dependence of the histogram on wind speed only or precipitation only, respectively. For this general (or 'all' condition) case, observations are excluded if either the precipitation or the wind is zero or in the weakest 10% of the non-zero values, as the focus here is on the extreme portions of the distributions. The
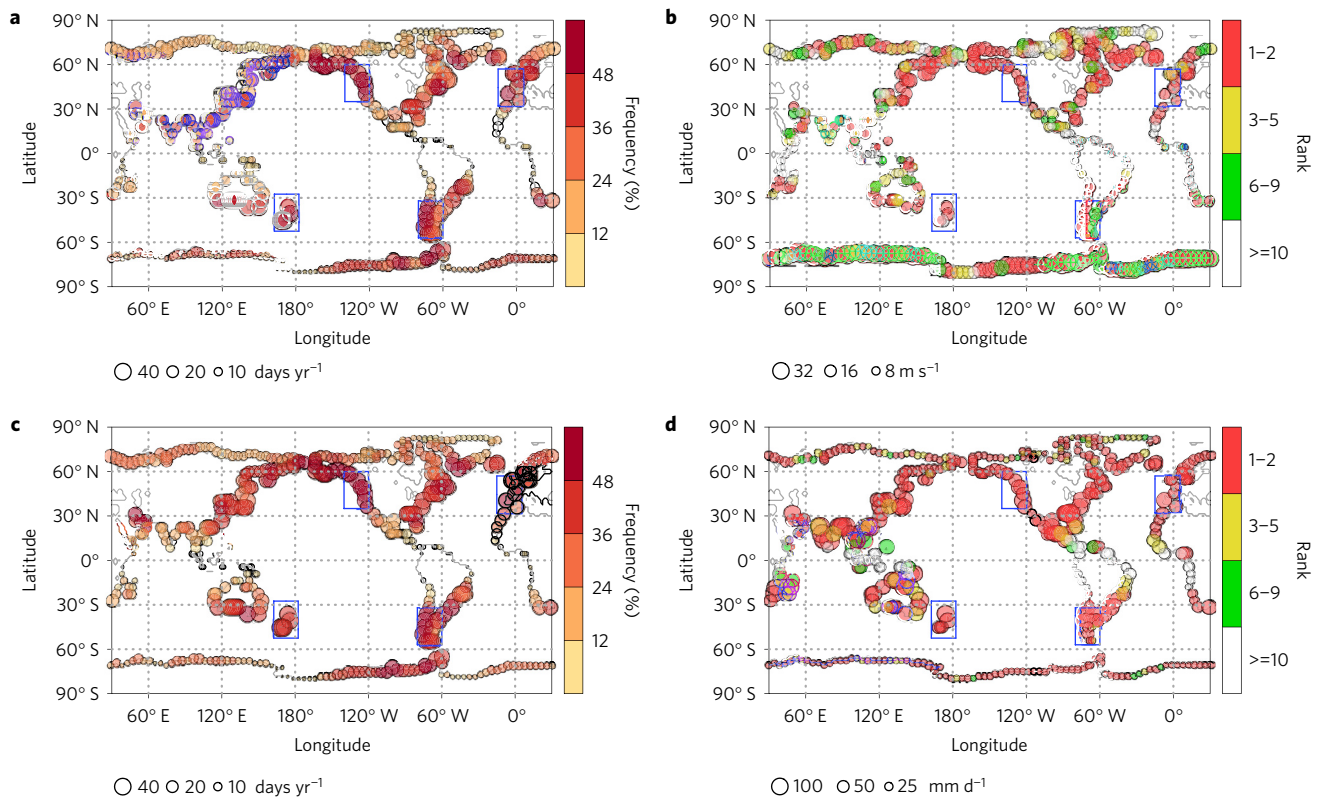
Figure 2 | ARs and coastal wind/precipitation extremes. a, Fraction of wind extremes associated with ARs at the coastal pixels (shading; based on the information in Fig. 1b). Also shown is the frequency of AR occurrence out of all times at each pixel (size of the circles; based on the information in Fig. 1a). **b,** The highest rank (shading) and 10-m wind speed (m s^{-1}; size of the circles) of AR-related wind extreme. **c,d,** As **a,b** but for precipitation extremes. The four blue boxes outline the regions used in subsequent analysis. In **a** and **c**, values are shaded only if statistically significant at the 99% level.
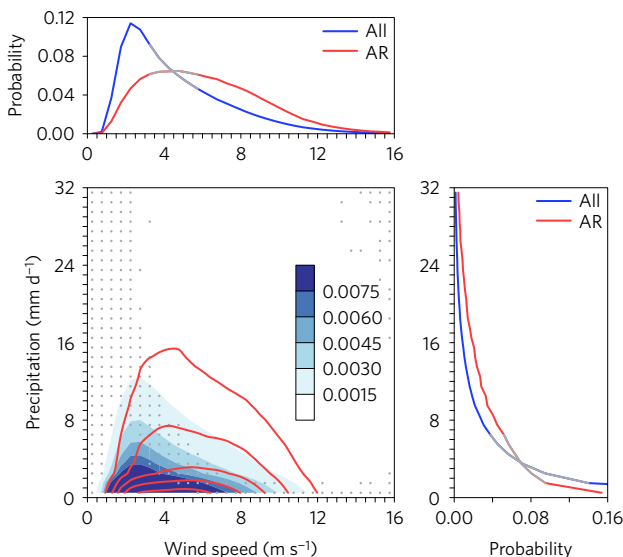

Figure 3 | Probability distribution of wind speed/precipitation. Bottom left: joint histogram of 10-m wind speed (m s^{-1}) versus precipitation (mm d^{-1}) combining coastal pixels from four regions (outlined in Fig. 2). Observations are excluded if either precipitation or wind speed is zero or among the weakest 10% of non-zero values. The blueish shading is for all wet days. Blue lines in the line plots above (to the right) are a sum across precipitation (wind speed). The red contours (using the same contouring level) and red lines are the counterpart for the AR subset (for example, the subset of the small black boxes within the green contours in Supplementary Fig. 2). Grey lines or stippling indicate where the difference between the two histograms is statistically insignificant at the 99% level.

red contours and lines show the same information but considering only AR conditions. The joint distribution for all conditions (that is, blue shading) emphasizes a log-normal character with respect to precipitation[33], and a more Gaussian distribution, albeit with positive skew, with respect to wind speed. Under AR conditions (red contours), the frequency distribution shifts markedly towards higher wind speed and precipitation values. Comparing the histograms in the upper line plot illustrates that the most probable wind value for all conditions roughly doubles, from ∼2 m s^{-1} to ∼4 m s^{-1}. In addition, for a rare event with probability 0.02, the extreme value for the all conditions is on the order of 8 m s^{-1}, whereas for AR conditions it is 12 m s^{-1}. Similarly, comparing the histograms in the right line plot illustrates that an event at the 0.02 level changes from 8 mm d^{-1} to over 16 mm d^{-1}. Or, put another way, the histograms show that AR conditions are associated with an approximate doubling of the most typical surface wind speed and a 50–100% increase in the wind and precipitation values for extreme cases (for example, probability of 0.02).

Socio-economic considerations

Although the societal impacts of AR precipitation extremes have been considered in a number of studies through the examination of their relationship to flooding[2,3,6,11,19,21,34], here we illustrate their impacts by considering potential wind damage and actual insured losses due to wind damage. Figure 4a–c shows histograms of global 10-m wind strengths, categorized in terms of the Beaufort Wind Scale (BWS)[35] (see also https://en.wikipedia.org/wiki/Beaufort_scale and references therein), for each grid cell over land, along coastlines, and over oceans, respectively, with the blue dots representing all grid cells sampled—that is, regardless of the presence/absence of ARs—and the red dots representing the subset of grid cells within detected AR boundaries. The BWS is a mapping
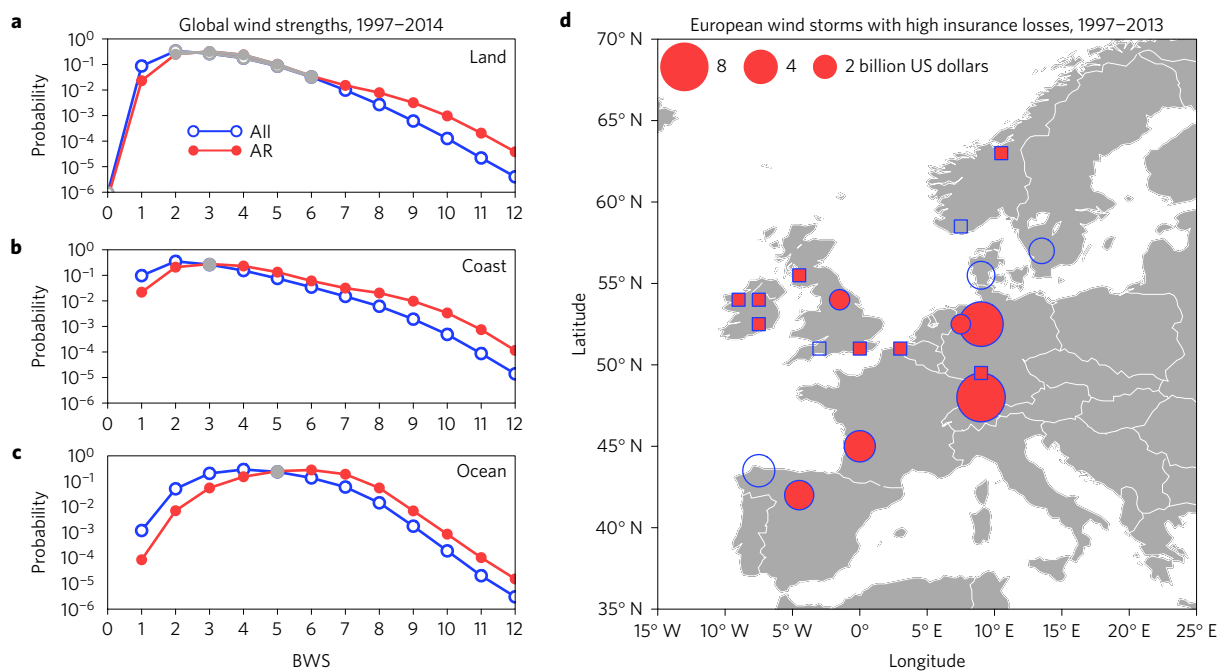
Figure 4 | Socio-economic impacts of wind extremes. a–c, Histograms of global 10-m wind strengths, in terms of their value on the BWS[35], over each grid cell over land (**a**), along coastlines (**b**) and over oceans (**c**), with the blue dots representing all grid cells sampled, and the red dots the subset of grid cells within detected AR boundaries. Grey dots indicate where the difference between the two histograms is statistically insignificant at the 99% level. **d**, Insurance losses associated with European wind storms (size of blue outlined circles). The blue outlined squares indicate losses less than 1 billion US dollars or data not available. Red fills indicate cases for which ARs are present at the grid cell with the highest local rank of wind speed (where the circles/squares are drawn).

between wind speed ranges and a numeric scale from 0–12, with each successive value associated with increasing impacts/damage, considering wave height, sea state and land conditions. For example, a BWS of 8 indicates gale force winds of 17.2–20.7 m s^{-1}, wave heights of 5.5–7.5 m, and a set of qualitative indicators of sea state and typical damage experienced over land (for example, broken trees, high waves, structural damage). These histograms indicate that, under AR conditions, the frequency of threatening/damaging winds (that is, BWS ∼8–12) is larger, by factors ranging up to ten, than the unconditional frequency of these events without considering the presence/absence of ARs; this is particularly true near coasts and over land. To put the above considerations of extreme wind damage in economics terms, Fig. 4d illustrates that ARs are associated with 14 of 19 (the fraction is significantly larger than by chance with $P < 0.01$; see Methods) recently analysed large European wind storm insurance losses from 1997–2013[36], with a number of the losses exceeding 2 billion US dollars.

The objective of our study was to expand the consideration of AR impacts by quantifying their association with near-surface wind extremes and precipitation extremes, extending these considerations to a global perspective[23], and with particular attention on AR landfalls at the world's coastlines. Our results illustrate associations between ARs and precipitation and wind extremes across the globe. Although the relationships between ARs and precipitation extremes have been studied in a limited number of regions, this study has extended these relationships to a global scale. Most uniquely, our results illustrate a close association between ARs and global wind extremes, and further highlight the potential socio-economic impacts of these extremes. Suggestions for future research include further characterization of these connections, bearing in mind local environmental, economic and topographic conditions, to specific wind-related hazards, such as storm surge and coastal flooding, wind damage, marine weather and significant wave height[26,28].

Methods

Methods, including statements of data availability and any associated accession codes and references, are available in the [online version of this paper](#).

References

1. Zhu, Y. & Newell, R. E. Atmospheric rivers and bombs. *Geophys. Res. Lett.* **21**, 1999–2002 (1994).
2. Ralph, F. M. & Dettinger, M. D. Storms, floods, and the science of atmospheric rivers. *Eos* **92**, 265–266 (2011).
3. Dettinger, M. D. & Ingram, B. L. The coming megafloods. *Sci. Am.* **308**, 64–71 (2013).
4. Gimeno, L. *et al.* Major mechanisms of atmospheric moisture transport and their role in extreme precipitation events. *Annu. Rev. Environ. Resour.* **41**, 117–141 (2016).
5. Ralph, F. M. *et al.* CalWater field studies designed to quantify the roles of atmospheric rivers and aerosols in modulating U.S. west coast precipitation in a changing climate. *Bull. Am. Meteorol. Soc.* **97**, 1209–1228 (2016).
6. Dettinger, M. D., Ralph, F. M., Das, T., Neiman, P. J. & Cayan, D. R. Atmospheric rivers, floods and the water resources of California. *Water* **3**, 445–478 (2011).
7. Rutz, J. J., Steenburgh, W. J. & Ralph, F. M. Climatological characteristics of atmospheric rivers and their inland penetration over the western United States. *Mon. Rev.* **142**, 905–921 (2014).
8. Neiman, P. J. *et al.* The landfall and inland penetration of a flood-producing atmospheric river in Arizona. Part I: observed synoptic-scale, orographic, and hydrometeorological characteristics. *J. Hydrometeorol.* **14**, 460–484 (2013).
9. Lavers, D. A. & Villarini, G. The nexus between atmospheric rivers and extreme precipitation across Europe. *Geophys. Res. Lett.* **40**, 3259–3264 (2013).
10. Guan, B., Molotch, N. P., Waliser, D. E., Fetzer, E. J. & Neiman, P. J. The 2010/11 snow season in California's Sierra Nevada: role of atmospheric rivers and modes of large-scale variability. *Wat. Resour. Res.* **49**, 1–13 (2013).
11. Lavers, D. A. *et al.* Future changes in atmospheric rivers and their implications for winter flooding in Britain. *Environ. Res. Lett.* **8**, 034010 (2013).

12. Dettinger, M. Climate change, atmospheric rivers, and floods in California - a multimodel analysis of storm frequency and magnitude changes. *J. Am. Water Resour. Assoc.* **47,** 514–523 (2011).
13. Gao, Y., Lu, J. & Leung, R. Uncertainties in projecting future changes in atmospheric rivers and their impacts on heavy precipitation over Europe. *J. Clim.* **29,** 6711–6726 (2016).
14. Guan, B. & Waliser, D. E. Detection of atmospheric rivers: evaluation and application of an algorithm for global studies. *J. Geophys. Res.* **120,** 12514–12535 (2015).
15. Hagos, S. M., Leung, L. R., Yoon, J.-H., Lu, J. & Gao, Y. A projection of changes in landfalling atmospheric river frequency and extreme precipitation over western North America from the large ensemble CESM simulations. *Geophys. Res. Lett.* **43,** 1357–1363 (2016).
16. Nayak, M. A., Villarini, G. & Lavers, D. A. On the skill of numerical weather prediction models to forecast atmospheric rivers over the central United States. *Geophys. Res. Lett.* **41,** 4354–4362 (2014).
17. Lavers, D. A., Pappenberger, F. & Zsoter, E. Extending medium-range predictability of extreme hydrological events in Europe. *Nat. Commun.* **5,** 5382 (2014).
18. Wick, G. A., Neiman, P. J., Ralph, F. M. & Hamill, T. M. Evaluation of forecasts of the water vapor signature of atmospheric rivers in operational numerical weather prediction models. *Weath. Forecast.* **28,** 1337–1352 (2013).
19. Ralph, F. M. *et al.* Flooding on California's Russian River: role of atmospheric rivers. *Geophys. Res. Lett.* **33,** L13801 (2006).
20. Ralph, F. M. & Dettinger, M. D. Historical and national perspectives on extreme west coast precipitation associated with atmospheric rivers during December 2010. *Bull. Am. Meteorol. Soc.* **93,** 783–790 (2011).
21. Neiman, P. J., Schick, L. J., Ralph, F. M., Hughes, M. & Wick, G. A. Flooding in western Washington: the connection to atmospheric rivers. *J. Hydrometeorol.* **12,** 1337–1358 (2011).
22. Waliser, D. E. *et al.* The "year" of tropical convection (May 2008 to April 2010): climate variability and weather highlights. *Bull. Am. Meteorol. Soc.* **93,** 1189–1218 (2012).
23. Martius, O., Pfahl, S. & Chevalier, C. A global quantification of compound precipitation and wind extremes. *Geophys. Res. Lett.* **43,** 7709–7717 (2016).
24. Raveh-Rubin, S. & Wernli, H. Large-scale wind and precipitation extremes in the Mediterranean: a climatological analysis for 1979–2012. *Q. J. R. Meteorol. Soc.* **141,** 2404–2417 (2015).
25. Fink, A. H., Brücher, T., Ermert, V., Krüger, A. & Pinto, J. G. The European storm Kyrill in January 2007: synoptic evolution, meteorological impacts and some considerations with respect to climate change. *Nat. Hazards Earth Syst. Sci.* **9,** 405–423 (2009).
26. Quevauviller, P. *Hydrometeorological Hazards: Interfacing Science and Policy* (Wiley, 2014).
27. Khouakhi, A. & Villarini, G. On the relationship between atmospheric rivers and high sea water levels along the U.S. west coast. *Geophys. Res. Lett.* **43,** 8815–8822 (2016).
28. Klawa, M. & Ulbrich, U. A model for the estimation of storm losses and the identification of severe winter storms in Germany. *Nat. Hazards Earth Syst. Sci.* **3,** 725–732 (2003).
29. Neiman, P. J. *et al.* Diagnosis of an intense atmospheric river impacting the Pacific northwest: storm summary and offshore vertical structure observed with COSMIC satellite retrievals. *Mon. Weath. Rev.* **136,** 4398–4420 (2008).
30. Dee, D. P. *et al.* The ERA-Interim reanalysis: configuration and performance of the data assimilation system. *Q. J. R. Meteorol. Soc.* **137,** 553–597 (2011).
31. *Wave Forecast Verification* (Joint WMO-IOC Technical Commission for Oceanography and Marine Meteorology, 2016); http://www.jcomm.info/index.php?option=com_content&view=article&id=131&Itemid=37
32. Ranjha, R., Svensson, G., Tjernström, M. & Semedo, A. Global distribution and seasonal variability of coastal low-level jets derived from ERA-Interim reanalysis. *Tellus* **65,** 20412 (2013).
33. Liu, Y., Zhang, W., Shao, Y. & Zhang, K. A comparison of four precipitation distribution models used in daily stochastic models. *Adv. Atmos. Sci.* **28,** 809–820 (2011).
34. Guan, B., Waliser, D. E., Ralph, F. M., Fetzer, E. J. & Neiman, P. J. Hydrometeorological characteristics of rain-on-snow events associated with atmospheric rivers. *Geophys. Res. Lett.* **43,** 2964–2973 (2016).
35. Saucier, W. J. *Principles of Meteorological Analysis* (Dover Publications, 2003).
36. Roberts, J. F. *et al.* The XWS open access catalogue of extreme European windstorms from 1979 to 2012. *Nat. Hazards Earth Syst. Sci.* **14,** 2487–2501 (2014).

Acknowledgements

Author contributions

D.W. contributed the concept for the study, provided guidance on analysis and interpretation of results and figures, and contributed the majority of the writing. B.G. contributed all of the data analysis, provided guidance on analysis and interpretation of results and figures, and contributed to the writing.

Additional information

Supplementary information is available in the online version of the paper. Reprints and permissions information is available online at www.nature.com/reprints. Correspondence and requests for materials should be addressed to D.W.

Competing financial interests

The authors declare no competing financial interests.

Methods

For this study, ARs are defined via a recently developed global detection algorithm based on IVT[14]. The data set used for both IVT and 10-m wind is the ECMWF Interim reanalysis[30] (ERA-Interim), which provides global, 6-hourly atmospheric fields at 1.5° × 1.5° spatial resolution. AR detection is based on IVT derived from specific humidity and wind fields at 17 pressure levels between 1,000 and 300 hPa inclusive. The land–sea mask from the same data set, and coastal grid cells based on the land–sea mask, are used in part of the analysis. Daily precipitation from the 1° × 1° resolution Global Precipitation Climatology Project version 1.2 is used to quantify the impacts of ARs on global precipitation patterns. This data set is produced by optimally merging satellite retrievals and gauge analyses[37] and is re-gridded to the ERA-Interim resolution. Socio-economic impacts of ARs are understood by considering the categorization of wind speed values according to the BWS[35] as well as a catalogue of European extreme wind storms that includes associated insurance losses[36]. Here we point out that, although analyses involving wind damage are often carried out in terms of wind force or power (typically involving the square or cube of wind speed)[38], the manner in which we do our analyses (that is, basing the calculations on percentiles and/or rankings of wind speed) determines that the findings associated with our analysis are qualitatively the same whether we consider wind speed or a higher moment of wind speed. The period of the analysis is 1997–2014.

The procedure for identifying and characterizing ARs can be summarized as two main steps: extraction of the original set of 'objects' based on the IVT magnitude threshold at each grid cell; and application of the IVT direction, length, and length/width ratio criteria to these objects, resulting in a defined set of ARs. Only a brief summary of the criteria are provided here; their motivation, sensitivity considerations and further details are given in the complete algorithm and application description[14]. For the first step, the IVT threshold is the value of the 85% percentile based on the IVT distribution for the given spatial location and month of the year, and being at least $100 \, \text{kg} \, \text{m}^{-1} \, \text{s}^{-1}$. For the second step, there is a requirement for coherence in the overall IVT direction within the identified object and there to be an appreciable northward component (that is, $50 \, \text{kg} \, \text{m}^{-1} \, \text{s}^{-1}$). In addition, there is a requirement for the identified ARs to have length greater or equal to 2,000 km and a length-to-width ratio greater or equal to 2. The upper panel of Supplementary Fig. 1 shows the result for an arbitrary 6 h time step after all the above AR detection criteria have been applied, with each object labelled by a unique colour. The lower panel of Supplementary Fig. 1 shows specific details of the AR making landfall in western North America, including the AR shape boundary (green contour), IVT (shading), 10-m wind (arrows), and surface precipitation (blue contours). For any given AR, only wind and precipitation within the AR shape boundary are considered associated with the AR and included for calculation of AR fractions shown in Fig. 1.

Wind and precipitation extremes at each grid cell are defined as values exceeding the 98th percentile[28] specific to that grid cell (see Supplementary Figs 3 and 4). The percentile is based on all months during the analysis period, and only non-zero values are included in calculating the percentile. Supplementary Fig. 2 shows the additional details associated with assigning the associated wind and precipitation values at landfall by zooming in on two ARs shown in Supplementary Fig. 1 as examples. Here, the AR shape boundary is shown by the green contour, and the IVT magnitude in grey shading. In the western North America case, the AR landfall is associated with wind extremes at ∼1/2 of the intersecting coastal grid cells (IVT direction/magnitude in red arrows), and precipitation extremes at ∼1/3 of the intersecting coastal grid cells (purple dots). In the southern South America case, the AR landfall is associated with a wind extreme at one grid cell on the west coast—that is, the side of the landfall—with no precipitation extreme in this case.

Statistical significance of the results presented in each figure is evaluated by Monte Carlo simulations. In each case, an empirical distribution of the test statistic is formed by randomly resampling the input data in space and time with 2,000 iterations. The P value is then calculated based on comparing the observed value of the test statistic against its empirical distribution. Statistical significance is inferred if $P < 0.01$ based on a two-tailed test.

Code availability. The MATLAB code for the AR detection algorithm is available from the corresponding author upon request.

Data availability. The following data were obtained freely online: ERA-Interim: http://apps.ecmwf.int/datasets/data/interim-full-daily
GPCP: ftp://meso.gsfc.nasa.gov/pub/1dd-v1.2.
European extreme wind storms catalogue:
http://www.europeanwindstorms.org.
The global AR catalogue based on ERA-Interim and the detection algorithm described in ref. 14 is available at https://ucla.app.box.com/v/arcatalog.

References

37. Huffman, G. J. *et al*. Global precipitation at one-degree daily resolution from multisatellite observations. *J. Hydrometeorol.* **2**, 36–50 (2001).
38. Hanley, J. & Caballero, R. The role of large-scale atmospheric flow and Rossby wave breaking in the evolution of extreme windstorms over Europe. *Geophys. Res. Lett.* **39**, L21708 (2012).